24. Gaarde, M. B. & Schafer, K. J. Space-time considerations in the phase locking of high harmonics. *Phys. Rev. Lett.* **89,** 213901 (2002).
25. Constant, E., Mével, E., Zaÿr, A., Bagnoud, V. & Salin, F. Toward sub-femtosecond pump–probe experiments: A dispersionless autocorrelator with attosecond resolution. *J. Phys. IV Fr.* **11,** Pr2-537–Pr2-540 (2001).
26. Mashiko, H., Suda, A. & Midorikawa, K. All-reflective interferometric autocorrelator for the measurement of ultra-short optical pulses. *Appl. Phys. B* **76,** 525–530 (2003).
27. Sekikawa, T., Katsura, T., Miura, S. & Watanabe, S. Measurement of the intensity-dependent atomic dipole phase of a high harmonic by frequency-resolved optical gating. *Phys. Rev. Lett.* **88,** 193902 (2002).
28. Muller, H. G. Reconstruction of attosecond harmonic beating by interference of two-photon transitions. *Appl. Phys. B* **74** (suppl.), S17–S21 (2002).
29. Quéré, F., Itatani, J., Yudin, G. L. & Corkum, P. B. Attosecond spectral shearing interferometry. *Phys. Rev. Lett.* **90,** 073902 (2003).
30. Norin, J. *et al.* Time-frequency characterization of femtosecond extreme ultraviolet pulses. *Phys. Rev. Lett.* **88,** 193901 (2002).

Acknowledgements The experiment was performed using the ATLAS laser facility at the Max-Planck-Institut für Quantenoptik, Garching. This work is supported in part by the European Community's Human Potential Programmes, Generation and Characterisation of Attosecond Pulses in Strong Laser-Atom Interactions: A Step towards Attophysics (ATTO) and the Ultraviolet Laser Facility (ULF).

Competing interests statement The authors declare that they have no competing financial interests.

Correspondence and requests for materials should be addressed to G.D.T. (george.tsakiris@mpq.mpg.de).

Drying-mediated self-assembly of nanoparticles

Eran Rabani[1], David R. Reichman[2], Phillip L. Geissler[3]* & Louis E. Brus[4]

[1]*School of Chemistry, Tel Aviv University, Tel Aviv 69978, Israel*
[2]*Department of Chemistry and Chemical Biology, Harvard University, Cambridge, Massachusetts 02138, USA*
[3]*Department of Chemistry, Massachusetts Institute of Technology, Cambridge, Massachusetts 02139, USA*
[4]*Department of Chemistry, Columbia University, 3000 Broadway, New York, New York 10027, USA*

* Present address: Department of Chemistry, University of California, Berkeley, California 94720, USA

Systems far from equilibrium can exhibit complex transitory structures, even when equilibrium fluctuations are mundane[1,2]. A dramatic example of this phenomenon has recently been demonstrated for thin-film solutions of passivated nanocrystals during the irreversible evaporation of the solvent[3–14]. The relatively weak attractions between nanocrystals, which are efficiently screened in solution, become manifest as the solvent evaporates, initiating assembly of intricate, slowly evolving structures[4]. Although certain aspects of this aggregation process can be explained using thermodynamic arguments alone[6], it is in principle a non-equilibrium process[7]. A representation of this process as arising from the phase separation between a dense nanocrystal 'liquid' and dilute nanocrystal 'vapour' captures some of the behaviour observed in experiments[3], but neglects entirely the role of solvent fluctuations, which can be considerable on the nanometre length scale[15]. Here we present a coarse-grained model of nanoparticle self-assembly that explicitly includes the dynamics of the evaporating solvent. Simulations using this model not only account for all observed spatial and temporal patterns, but also predict network structures that have yet to be explored. Two distinct mechanisms of ordering emerge, corresponding to the homogeneous and heterogeneous limits of evaporation dynamics. Our calculations show how different choices of solvent, nanoparticle size (and identity) and thermodynamic state give rise to the various morphologies of the final structures. The resulting guide for designing statistically patterned arrays of nanoparticles suggests the possibility of fabricating spontaneously organized nanoscale devices.

In our model, the solvent is represented as a two-dimensional lattice gas[16]. In detail, each cell of a square lattice, with the size of the solvent's correlation length, $\xi \approx 1$ nm, is occupied by either liquid ($l_i = 1$) or vapour ($l_i = 0$), where l_i is a binary variable roughly proportional to solvent density at lattice site i. Adjacent liquid cells attract one another with a strength ϵ_l determined by the energy density of the fluid. The chemical potential, μ, and temperature, T, of a surrounding bath (in experiments, the overlying vapour) establish the average concentration of liquid and vapour cells at equilibrium. We consider non-equilibrium conditions appropriate for experiments conducted in a closed chamber, in which small amounts of solvent may remain on the surface long after the majority has evaporated. Initially, the lattice is entirely filled with liquid and nanoparticles. But μ is fixed at a value for which the equilibrium state is vapour. Although the subsequent decay of solvent density is neither constant nor simply exponential for this choice of ensemble, we find that it is well characterized by a single timescale. (See Supplementary Information.)

A cell of the lattice that is not occupied by liquid may instead be occupied by a nanoparticle. This fact, together with attractions between neighbouring liquid and nanoparticles (of strength ϵ_{nl}), can alter the drying dynamics significantly. We use a second set of binary variables, n_i, to describe nanoparticle density on the lattice. Where nanoparticles exclude solvent, $n_i = 1$, and elsewhere, $n_i = 0$. Because the size of a nanoparticle, d, can exceed the range of correlated solvent fluctuations, we allow them to span several cells of the lattice. Adjacent nanoparticle cells attract one another, with strength ϵ_n, so that they tend to aggregate in the absence of liquid. The geometry and relevant length scales of this lattice model are sketched in Fig. 1.

The dynamics of our model are stochastic, both for fluctuations in solvent density and for nanoparticle diffusion. In the former case, configurations evolve by Monte Carlo dynamics. We attempt to convert a randomly chosen lattice cell, i, from liquid to vapour (or vice versa), $l_i \rightarrow (1 - l_i)$. This perturbation is accepted with a

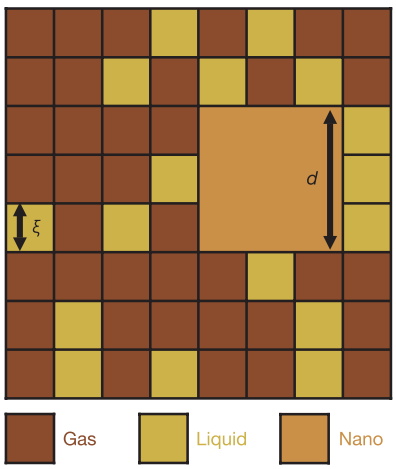

Figure 1 A sketch of the square lattice and important length scales of our mesoscopic model. Each lattice cell of size ξ is occupied by gas, liquid or nanoparticle. The colour scheme shown is maintained in subsequent figures. For results in those figures, we have taken $\epsilon_n = 2\epsilon_l$ and $\epsilon_{nl} = 1.5\epsilon_l$, for which nanoparticles are well solvated before evaporation. The lattice comprises 1,000 × 1,000 cells unless otherwise stated, and each nanoparticle spans 4 × 4 cells. (As observed in experiments[3,4], the qualitative results of our model are not sensitive to the size of the nanoparticles.)

Metropolis probability, $p_{acc} = \min [1, \exp(-\Delta H/k_B T)]$, where k_B is Boltzmann's constant, and ΔH is the resulting change in energy. For a particular configuration of $\{l_i\}$ and $\{n_i\}$:

$$H = -\epsilon_l \sum_{\langle ij \rangle} l_i l_j - \epsilon_n \sum_{\langle ij \rangle} n_i n_j - \epsilon_{nl} \sum_{\langle ij \rangle} n_i l_j - \mu \sum_i l_i \qquad (1)$$

The first three summations in equation (1) include only adjacent lattice cells. These dynamics do not conserve solvent density within the film, as seems appropriate for the experiments under study. Nanocrystals, on the other hand, have negligible vapour pressure, and their surface density should be locally conserved. In our model, nanoparticles execute a random walk on the lattice, biased by their interactions with liquid cells and with each other. We attempt to displace a nanoparticle by a single lattice spacing in a randomly chosen direction. Such a move is accepted also with the above Metropolis probability, but only if the region into which the nanoparticle moves is completely filled with liquid. Solvent density in lattice cells overtaken by this displacement is regenerated in the wake of the moving nanoparticle. This final constraint mimics the very low mobility of nanocrystals on a dry surface. It also provides an additional coupling between the kinetics of evaporation and nanoparticle phase separation.

In the absence of solvent fluctuations, our model of nanoparticle self-assembly is related to simple models of coarsening that have been studied extensively in the contexts of ferromagnetic phase-ordering and spinodal decomposition[1,2]. When, for example, an Ising magnet is quenched below its critical temperature, amorphous but nearly homogeneous domains form rapidly and then coalesce. This union of ever-larger domains proceeds in essentially the same way at each stage, but with a growing characteristic length scale, $R(t)$. The coarsening is thus self-similar, and $R(t)$ evolves as $R \approx t^{\alpha}$. Exponents for this dynamical power law depend on the nature of dynamics and physical constraints[1].

Our model should reflect this basic phenomenology in certain limits of the parameters controlling solvent evaporation and nanoparticle aggregation. The appropriate limit is not one of instantaneous evaporation, because nanoparticles are immobile in the absence of solvent. We find that simple coarsening behaviour is instead realized when evaporation is spatially homogeneous while the boundaries of nanoparticle domains remain fluxional throughout the growth dynamics. The latter condition requires that boundaries are wet (that is, covered with solvent) and that the energetic cost of moving a nanoparticle into the surrounding solvent is comparable to $k_B T$. In this limit the scarcity of solvent drives aggregation of nanoparticles uniformly, while growing domains are free to rearrange and conglomerate. We expect this scenario when the solvent is near the spinodal limit of metastability, $\mu \approx \mu_{sp}(T)$, while a wetting layer remains thermally stable at the edges of nanoparticle domains, $\mu + \epsilon_{nl} + \epsilon_l > k_B T$.

A survey of aggregate morphologies obtained in this limit of homogeneous drying is provided in Fig. 2. The lower panels show snapshots from simulated non-equilibrium trajectories, at intermediate times. The chosen trajectories differ from one another only in coverage (that is, mean surface density) and mobility of nanoparticles. At low coverage (Fig. 2a), distinct, disk-like aggregates of

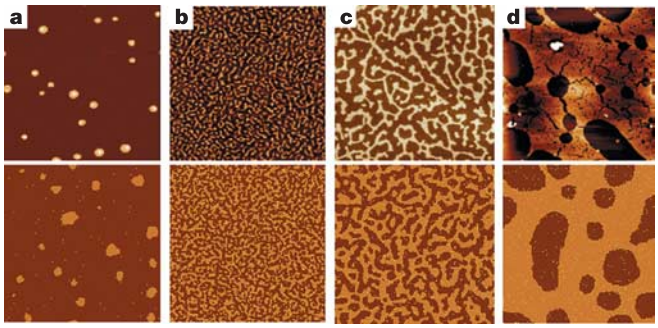

Figure 2 Self-assembled morphologies resulting from homogeneous evaporation and wetting of nanoparticle domains. The lower panels show results of model simulations for coverages of 5% (**a**), 30% (**b**), 40% (**c**) and 60% (**d**). In all cases $k_B T = \epsilon_l/2$ and $\mu = -2.25\epsilon_l$. ($\mu = -2\epsilon_l$ corresponds to phase coexistence of liquid and vapour.) Although the characteristic times of evaporation, τ, and nanoparticle diffusion, τ_D, are increasing functions of coverage, their ratio, $\tau/\tau_D \approx 200$, is nearly constant. The size of the domains is largely determined by the nanoparticle mobility and the time window, τ_s, before growth is stopped. Disks containing several hundred nanoparticles form for the lowest coverage at $\tau_s/\tau \approx 2{,}500$. In **b**, small domains form at $\tau_s/\tau \approx 4$. Larger aggregates appear by $\tau_s/\tau \approx 50$ and $\tau_s/\tau \approx 500$ in **c** and **d**, respectively. The upper panels show corresponding experimentally observed morphologies for CdSe nanocrystals at similar coverages. Solvents used in these experiments range from hexane (**a** and **c**) to chloroform (**b**) and a 90:10 mixture of chloroform and methanol (**d**). Comparison with simulation results is therefore strictly qualitative.

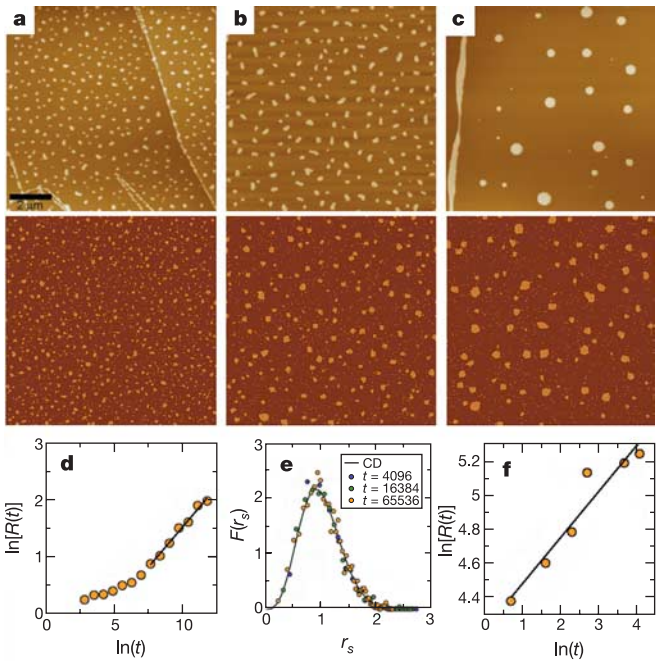

Figure 3 Dynamics of nanoparticle assembly at low coverage. **a**–**c**, The lower panels show simulation results for the same thermodynamic state as in Fig. 2, with a time range of $\tau_s = 15\tau$ (**a**) to $\tau_s = 600\tau$ (**c**). The upper panels depict experimental results for PbSe nanocrystals in octane, with a range of $\tau_s = 2$ min (**a**) to $\tau_s = 60$ min (**c**) in the time elapsed before sudden exposure to the atmosphere induced complete drying. In calculations, evaporation is slow compared to nanoparticle mobility, $\tau/\tau_D \approx 1{,}000$. We assign a physical timescale, Δt, to a single Monte Carlo step in our simulations by identifying the mean squared displacement of a nanoparticle (under non-evaporating conditions) after m steps as $4D_{exp}m\Delta t$, where D_{exp} is a diffusion coefficient estimated from experimental data. With a physical length scale of $\xi = 1$ nm (yielding an overall scale of 1 μm for the depicted simulation boxes), the time dependence of domain growth in our model closely mirrors that of experiments. The very long timescales corresponding to the upper panels of (**a**–**c**) are not accessible by our simulations. A side-by-side comparison is made possible by the self-similar nature of these dynamics. The logarithm of the average domain size, $R(t)$, is plotted as a function of ln t for theory (**d**) and experiment (**f**). Solid lines, with slope 0.28 (**d**) and 0.27 (**f**), are best linear fits to the last several data points. Distributions of scaled disk sizes, $r_s = r/R(t)$, where r is the size of a particular disk, are plotted in **e** for several times, t, in the simulations depicted in **a**–**c**. Each distribution is averaged over several non-equilibrium trajectories. Assuming that disk mobility is proportional to $1/r$, cluster diffusion (CD) theory predicts the time-independent distribution shown in **e** as a solid line.

nanoparticles dominate the self-assembly. At higher coverage (Fig. 2b and c), nanoparticle domains are anisotropic and nearly percolate through the lattice. For very long times, however, even these fingering, high-coverage patterns tend toward large disks (Fig. 2d) and, asymptotically, to a single, macroscopic disk (not shown in the figure). Disk-like and ribbon-like morphologies thus represent different stages of the same growth mechanism.

The upper panels of Fig. 2 are micrographs of nanoparticle self-assembly in our experiments. In each case, the nanoparticle density lies within two per cent of the simulated system depicted in the adjacent panel, so that the dependence of pattern formation on coverage can be compared. With a reasonable estimate of the physical timescale for computed trajectories, the growth behaviour in simulation and experiment agree well. Comparing the detailed conditions of theory and experiment is made difficult by the lack of thermodynamic data for relevant thin-film solvents. We have been careful, however, to vary only those parameters that are changed or uncontrolled in the laboratory. Specifically, temperature, nanoparticle size and attraction are held fixed. The use of different solvents and evaporation conditions effectively adjusts chemical potential, nanoparticle mobility, and the attractions ϵ_l and ϵ_{nl}. We have chosen these model parameters within physically reasonable limits.

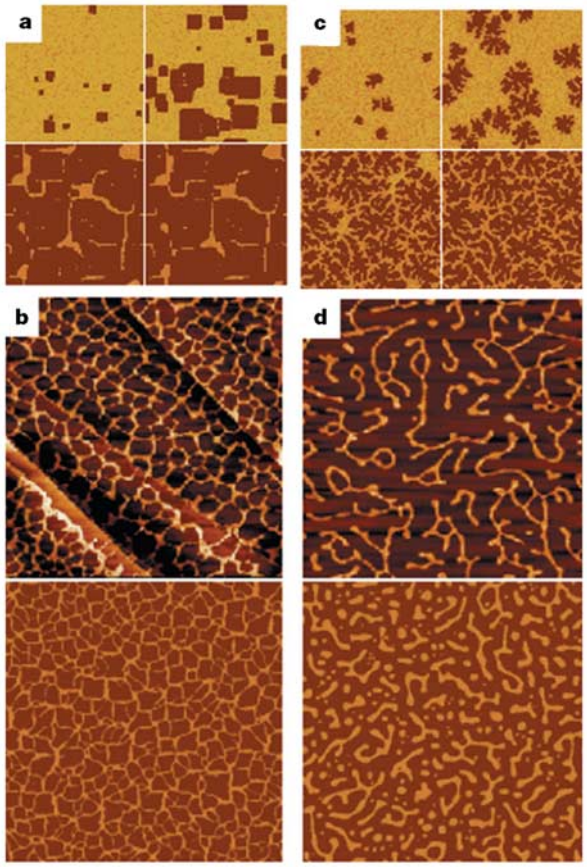

Figure 4 Self-assembled morphologies resulting from inhomogeneous evaporation in simulations and in experiments. Simulations were performed at the same temperature and chemical potential as in Fig. 2, but with stronger attractions between solvent cells, $\epsilon_l = 4k_BT$. Results are shown for coverages of 10% (**a**), 20% (**b**, bottom, and **d**, bottom), and 30% (**c**). In panels **a**–**c** the domain edges are not fluxional. Evaporation times are comparable in these cases, but nanoparticle mobility is varied significantly, yielding $\tau/\tau_D \approx 6{,}500$ in **a**, $\tau/\tau_D \approx 800$ in **b**, bottom, and $\tau/\tau_D \approx 150$ in **c**. A network structure observed in experiments with CdSe nanocrystals in hexane is shown **b**, top. The corresponding simulation result is shown in **b**, bottom. When domain edges remain fluxional following heterogeneous evaporation, cells break up as diffusion concentrates nanoparticle density at the nodes of the network, leaving distinct, worm-like domains as shown in **d**, bottom. In **d**, top, we show worm-like structures observed in experiments with CdSe nanocrystals in chloroform. The simulation results in **b** and **d** were obtained with a larger lattice (4,000 × 4,000).

The strong visual correspondence between the experimental and theoretical results in Fig. 2 demonstrates that our coarse-grained model successfully captures the qualitative dynamics of nanoparticle assembly in the limit of spatially homogeneous evaporation. A more quantitative comparison is illustrated in Fig. 3, depicting the time evolution of nanoparticle aggregation. Not only are coalescence and shape fluctuations visually similar, but the scaling of domain size with time is essentially identical. Following a transient period, $R(t)$ grows as t^{α} with $\alpha \approx 1/4$. This exponent is consistent with growth by cluster diffusion (in which domains grow solely by coalescence), assuming that cluster mobility scales as[17] R^{-1}. Figure 3e shows a more sensitive signature of this mechanism, namely, scaling behaviour of the cluster size distribution. These dynamics have been shown to dominate growth at intermediate times for a model similar to ours, but without solvent fluctuations or kinetic constraints[18]. We thus conclude that when evaporation is spatially uniform, the coarsening of nanoparticle domains is essentially that of an appropriate one-component fluid, as suggested in refs 3 and 4. Solvent evaporation simply triggers the onset of coarsening, after which the mechanism and timescale of growth are determined by nanoparticle diffusion.

When evaporation is instead strongly heterogeneous in space, the dynamics of self-assembly can be dramatically different. Between binodal and spinodal lines, $-2\epsilon_l > \mu > \mu_{sp}(T)$, solvent remains locally metastable on the surface. In this case phase change occurs not by long-wavelength fluctuations, but by nucleation and growth of vapour bubbles. At a given instant, the driving force for nanoparticle assembly therefore varies with position on the lattice. If nanoparticles are sufficiently mobile to track the fronts of growing vapour nuclei, their aggregate patterns will be shaped by the structural history of evaporation. Specifically, the locations of nanoparticle domains at long times should roughly trace the intersection lines of colliding vapour nuclei, leading to network-like morphologies. This assembly mechanism is similar in many respects to the Marangoni effect[19]. But in our model, the effective pinning of solutes to vapour fronts is not hydrodynamic in nature. Rather, it is a direct consequence of the coupling between two phase transitions, one in solvent density and the other in nanoparticle density.

Figure 4 shows a few representative simulation trajectories and experimental morphologies under conditions of heterogeneous evaporation. Figure 4a–c exemplifies network formation when domain edges are effectively frozen after evaporation, so that aggregation essentially halts when vapour nuclei meet. Each cell of the network structures in Fig. 4b and c thus marks an independent nucleation event whose front pushed nanoparticles to the boundaries of adjacent cells. The shapes of terminal structures in these trajectories are determined primarily by the relative timescales of evaporation, τ, and nanoparticle motion, $\tau_D = \xi^2/D$, where D is the nanoparticle diffusion coefficient in solution. For large τ/τ_D, the edges of nanoparticle domains may rearrange before the disappearance of solvent renders them immobile. The smooth edges of rod-like aggregates in Fig. 4a and of network cell boundaries in Fig. 4b are the result of such relaxation. By contrast, when τ/τ_D is small, domain edges are effectively frozen as they are formed, resulting in highly ramified networks such as that in Fig. 4c. The fractal-like appearance of these structures originates in dynamics that are locally similar to diffusion limited aggregation[20]. Attachment of nanoparticles to growing domains is nearly irreversible as the front of a vapour nucleus passes by. Strictly irreversible binding of random walkers is known to generate fractal structures. Cellular morphologies have been observed in several experiments[3,19,21]. One

such structure is depicted in the upper panel of Fig. 4b. It compares very well qualitatively with the model result shown in the lower panel of Fig. 4b.

When domain edges remain fluxional following heterogeneous evaporation, the networks described above for Fig. 4b are not stable, long-lived structures. Nanoparticles continue to move in this case, strongly biased by the interfacial tension of cell boundaries. Cells break up as diffusion concentrates nanoparticle density at the nodes of the network, leaving distinct, worm-like domains. An example of such a pattern generated by our simulations (lower panel of Fig. 4d) compares well with worm-like morphologies observed in experiments (upper panel of Fig. 4d). These structures are themselves transitory, because their anisotropy costs significant interfacial free energy. Domains thus eventually become disks, which diffuse and coalesce, as described in the case of homogeneous evaporation. This mechanism of network disintegration strongly resembles that observed in viscoelastic phase separation of a dynamically asymmetric mixture[2].

Our results suggest four basic regimes of drying-mediated nanoparticle assembly. They are distinguished by the spatial uniformity of solvent dynamics, and by the fluctuations of nanoparticle domain boundaries following evaporation. When solvent disappears homogeneously from the surface, disk-like or ribbon-like domains reminiscent of spinodal decomposition form at early times. We have shown that if these aggregates remain fluxional, they continue to evolve in a self-similar fashion, principally by diffusion and coalescence. If instead domain boundaries are frozen following evaporation, dynamical constraints arrest this growth at an early stage. When evaporation is inhomogeneous owing to infrequent nucleation events, network structures are formed at early times as vapour nuclei meet. These cellular patterns are only stable if interfaces are frozen following evaporation. Otherwise, networks fragment to form distinct domains that asymptotically evolve as in homogeneous coarsening.

Many aspects of these self-assembly mechanisms have previously been rationalized on the basis of seemingly distinct physical pictures. Our mesoscopic model unifies these pictures and provides a quantitative measure of their importance under different conditions. As such, it may serve as a basic guide for designing self-assembled structures with desired nanometre-scale features. Considering the simplicity of its energetics and dynamical rules, the degree of local order and anisotropy out of equilibrium is remarkable. We have omitted many physical details, most notably hydrodynamic convection, substrate roughness, non-local interactions, and film thickness. These effects can be added to provide microscopic realism, but it is interesting that they are not needed to account for the variety of patterns that have been observed in experiments. □

Received 9 May; accepted 25 September 2003; doi:10.1038/nature02087.

1. Bray, A. J. Theory of phase-ordering kinetics. *Adv. Phys.* **43,** 357–459 (1994).
2. Tanaka, H. Viscoelastic phase separation. *J. Phys. Condens. Matter* **12,** R207–R264 (2000).
3. Ge, G. & Brus, L. E. Evidence for spinodal phase in two-dimensional nanocrystal self-assembly. *J. Phys. Chem. B* **104,** 9573–9575 (2000).
4. Tang, J., Ge, G. & Brus, L. E. Gas-liquid-solid phase transition model for two-dimensional nanocrystal self-assembly on graphite. *J. Phys. Chem. B* **106,** 5653–5658 (2002).
5. Puntes, V. F., Krishnan, K. M. & Alivisatos, A. P. Colloidal nanocrystal shape and size control: The case of cobalt. *Science* **291,** 2115–2117 (2001).
6. Gelbart, W. M., Sear, R. P., Heath, J. R. & Chaney, S. Array formation in nano-colloids: Theory and experiment in 2D. *Farad. Disc.* **112,** 299–307 (1999).
7. Whitesides, G. M. & Grzybowski, B. Self-assembly at all scales. *Science* **295,** 2418–2421 (2002).
8. Murray, C. B., Kagan, C. R. & Bawendi, M. G. Self-organization of CdSe nanocrystallites into 3-dimensional quantum-dot superlattices. *Science* **270,** 1335–1338 (1995).
9. Freeman, R. G. *et al.* Self-assembled metal colloid monolayers—an approach to SERS substrates. *Science* **267,** 1629–1632 (1995).
10. Andres, R. P. *et al.* Self-assembly of a two-dimensional superlattice of molecularly linked metal clusters. *Science* **273,** 1690–1693 (1996).
11. Harfenist, S. A., Wang, Z. L., Alvarez, M. M., Vezmar, I. & Whetten, R. L. Highly oriented molecular Ag nanocrystal arrays. *J. Phys. Chem.* **100,** 13904–13910 (1996).
12. Sear, R. P., Chung, S. W., Markovich, G., Gelbart, W. M. & Heath, J. R. Spontaneous patterning of quantum dots at the air-water interface. *Phys. Rev. E* **59,** R6255–R6258 (1999).
13. Fried, T., Shemer, G. & Markovich, G. Ordered two-dimensional arrays of ferrite nanoparticles. *Adv. Mater.* **13,** 1158–1161 (2001).
14. Redl, F. X., Cho, K. S., Murray, C. B. & O'Brien, S. Three-dimensional binary superlattices of magnetic nanocrystals and semiconductor quantum dots. *Nature* **423,** 968–971 (2003).
15. Elbaum, M. & Lipson, S. G. How does a thin wetted film dry up? *Phys. Rev. Lett.* **72,** 3562–3565 (1994).
16. Chandler, D. *Introduction to Modern Statistical Mechanics* (Oxford Univ. Press, New York, 1987).
17. Ge, G. & Brus, L. E. Fast surface diffusion of large disk-shaped nanocrystal aggregates. *Nano Lett.* **1,** 219–222 (2001).
18. Lo, A. & Skoodje, R. T. Kinetic and Monte Carlo models of thin film coarsening: Cross over from diffusion-coalescence to Ostwald growth modes. *J. Chem. Phys.* **112,** 1966–1974 (2000).
19. Maillard, M., Motte, L., Ngo, A. T. & Pileni, M. P. Rings and hexagons made of nanocrystals: A Marangoni effect. *J. Phys. Chem. B* **104,** 11871–11877 (2000).
20. Witten, T. A. & Sander, L. M. Diffusion-limited aggregation, a kinetic critical phenomenon. *Phys. Rev. Lett.* **47,** 1400–1403 (1981).
21. Stowell, C. & Korgel, B. A. Self-assembled honeycomb networks of gold nanocrystals. *Nano Lett.* **1,** 595–600 (2001).

Supplementary Information accompanies the paper on **www.nature.com/nature**.

Acknowledgements This work was supported by the United States–Israel Binational Science Foundation. L.E.B. is supported by the Columbia MRSEC. P.L.G. was an MIT Science Fellow throughout most of this work. D.R.R. is a Sloan Fellow and Camille Dreyfus Teacher-Scholar.

Competing interests statement The authors declare that they have no competing financial interests.

Correspondence and requests for materials should be addressed to E.R. (rabani@tau.ac.il) or D.R.R. (reichman@chemistry.harvard.edu).

Proxy evidence for an El Niño-like response to volcanic forcing

J. Brad Adams[1], **Michael E. Mann**[1] **& Caspar M. Ammann**[2]

[1]*Department of Environmental Sciences, University of Virginia, Clark Hall, Charlottesville, Virginia 22903, USA*
[2]*Climate Global Dynamics Division, National Center for Atmospheric Research, 1850 Table Mesa Drive, Boulder, Colorado 80307-3000, USA*

Past studies have suggested a statistical connection between explosive volcanic eruptions and subsequent El Niño climate events[1,2]. This connection, however, has remained controversial[3–5]. Here we present support for a response of the El Niño/Southern Oscillation (ENSO) phenomenon[6,7] to forcing from explosive volcanism by using two different palaeoclimate reconstructions of El Niño activity[8,9] and two independent, proxy-based chronologies of explosive volcanic activity[5] from AD 1649 to the present. We demonstrate a significant, multi-year, El Niño-like response to explosive tropical volcanic forcing over the past several centuries. The results imply roughly a doubling of the probability of an El Niño event occurring in the winter following a volcanic eruption. Our empirical findings shed light on how the tropical Pacific ocean–atmosphere system may respond to exogenous (both natural and anthropogenic) radiative forcing.

Coupled ocean–atmosphere experiments have explored the possible response of ENSO to enhanced greenhouse gas concentrations[10–16]. Results indicate El Niño-like[11–14], neutral[15] and even La Niña-like[16] responses of average conditions (even a 'neutral' response represents a La Niña-like anomaly in the face of large-scale greenhouse warming). Simulations employing the Cane–Zebiak model of tropical Pacific coupled ocean–atmosphere dynamics, which exhibits a stronger dynamical feedback than most global models, produces negative (positive) eastern tropical Pacific sea surface temperature (SST) anomalies in response to a positive (negative) surface radiative forcing[17]. This imposes a La Niña-like cooling of the mean state in the presence of positive greenhouse warming[10]. It is intriguing in this context to reconsider the con-

